Role of orbital filling on nonlinear ionic Raman scattering in perovskite titanates

Mingqiang Gu and James M. Rondinelli

Role of Orbital Filling on Nonlinear Ionic Raman Scattering in Perovskite Titanates

Mingqiang Gu and James M. Rondinelli[*]

Department of Materials Science and Engineering,
Northwestern University, Evanston, IL 60208, USA
(Dated: December 15, 2016)

The linear and nonlinear phononic interactions between an optically excited infrared (IR) or hyper-Raman mode and a driven Raman mode are computed for the d^0 ($CaTiO_3$) and d^1 ($LaTiO_3$) titanates within a first-principles density functional framework. We calculate the potential energy surface expanded in terms of the A_g or B_{1g} mode amplitudes coupled to the A_u or the B_{3u} mode and determine the coupling coefficients for these multimode interactions. We find that the linear-quadratic coupling dominates the anharmonicities over the quadratic-quadratic interaction in the perovskite titanates. The IR and Raman modes both modify the electronic structure with the former being more significant but occurring on a different timescale; furthermore, the coupled-mode interactions lead to sizable perturbations to the valence bandwidth ($\sim 100\,meV$) and band gap ($\sim 50\,meV$). By comparing the coupling coefficients of undoped $CaTiO_3$ and $LaTiO_3$ to those for electron-doped ($CaTiO_3$) and hole-doped ($LaTiO_3$) titanates, we isolate the role of orbital filling in the nonlinear coupling process. We find that with increasing occupancy of the d manifold, the linear-quadratic interaction decreases by approximately 30% with minor changes induced by the cation chemistry (that mainly affect the phonon mode frequencies) or by electron correlation. We identify the importance of the Ti–O bond stiffness, which depends on the orbital filling, in governing the lattice anharmonicitiy. This microscopic understanding can be used to increase the nonlinear coupling coefficient to facilitate more facile access of nonequilibrium structures and properties through ionic Raman scattering processes.

PACS numbers: 78.47.J, 63.20.Ry, 71.20.Be

I. INTRODUCTION

Sub-band gap optical excitations can be used to drive materials into nonequilibrium excited states, which may exhibit nontrivial properties that cannot be observed in equilibrium structures defined by the chemistry of the constituent atoms.[1] Although ultrafast manipulation of magnetization in metal alloys[2,3] and oxides[4–7] using femtosecond pump-probe apparatuses have been studied for more than a decade, recent advances in optical sources,[8] make possible light-based control over matter within the field of nonlinear phononics.[9] The time scale for such processes ranges from 0.1–100 picoseconds (ps), depending on the relaxation (damping) of the phonon modes of the crystal, and is of the same order as the electron response time coupled to the ionic vibrations.[1,4,10,11] Recently, the phononic process has been shown experimentally[12] and subsequently theoretically[13] to alter the effective electron correlation strength (negative U), suggesting fascinating new routes to manipulate the strongly correlated systems.

Direct excitation of a single phonon, through for example, impulsive stimulated Raman scattering has been proposed as a possible path towards dynamical band gap control in correlated oxides.[14] On the other hand, nonlinear coupling between two phonons, *e.g.*, an infrared (IR) active and induced Raman modes, has been shown to melt orbital order and increase superconducting temperatures.[1,15–19] Among these processes, the nonlinear phononic coupling is of particular interest because a transient room-temperature superconducting state in Cu-based superconductors and K_3C_{60} has been demonstrated.[20] A recent study has theoretically identified the relationship of the nonlinear phononic process and

melting of the bond-density wave order, and how the excited state enhances superconductivity.[17] At the transient state the low frequency Raman phonon is strongly driven to a nonequilibrium amplitude, manifesting in a dynamically modulated Cu-O interlayer distance. Juraschek *et al* recently proposed the use of a two-laser-pump process to control the *phase* of the driven Raman mode, which is related to the sign of the coupling coefficient linking the IR and Raman modes, as an additional control parameter to tune the transient state.[21] A recent nonlinear phononics study of $PbTiO_3$ proposed selective phonon pumping as a plausible route to optically reverse the direction of the electric polarization in the ferroelectric, although the driving amplitude required was determined to be extremely high.[22] In pursuit of reducing the critical amplitudes necessary to realize light-induced transitions based on *nonlinear phononics*, we are motivated to study the microscopic origin of the size and sign of the anharmonic IR-Raman coupling interactions in complex oxides.

The mechanism of the nonlinear phonon pumping can be understood within a linear-quadratic mode coupling theory (see for example Ref. 23), between two normal modes of a crystal obeying IR and Raman selection rules. First a principal mode (usually an IR mode) is excited resonantly. That lattice excitation then applies a displacive force to all coupled Raman (R) modes along the normal mode coordinates. The response is nearly equivalent to that obtained from ionic Raman scattering (IRS),[24] in which the Raman mode typically rings when the pulse driving the IR mode has an envelope that is short compared to the frequency of the Raman mode;[25,26] in cases where the infrared mode is excited quasi-continuously, that is with an envelope that raises slowly compared to the frequency

of the Raman mode, then the Raman mode will displace but will not oscillate. In this limit, ionic Raman scattering is not strictly achieved and rather nonlinear phononics is a better description of the process. According to the theory of IRS, the coupling strength between the Raman and IR modes is determined by the allowed high order anharmonic term(s) present in the thermodynamic energy expanded as a function of normal-coordinate $\mathbf{Q}$. The energy expansion in terms of the amplitude Q for coupled $\mathbf{Q}_{IR}$ and $\mathbf{Q}_R$ phonons in a centrosymmetric material up to forth-order is

$$E = \frac{1}{2}\nu_R^2 Q_R^2 + \frac{1}{3}a_3 Q_R^3 + \frac{1}{4}a_4 Q_R^4 + \frac{1}{2}\nu_{IR}^2 Q_{IR}^2 + \frac{1}{4}b_4 Q_{IR}^4 + gQ_R Q_{IR}^2 + h_1 Q_R^2 Q_{IR}^2 + h_2 Q_R^3 Q_{IR} + h_3 Q_R Q_{IR}^3, \quad (1)$$

where $\nu_{R,IR}$ and $Q_{R,IR}$ are the frequencies and amplitudes of the Raman and IR modes, respectively. For a noncentrosymmetric group, a phonon mode can be simultaneously Raman- and IR-active; Eq. 1 then should be extended to include higher order interaction terms in order to capture the anharmonic feature of the polarized modes.[22]

According to group theory, the linear-quadratic interaction ($g \neq 0$) is allowed for the coupling between the A_g and the B_u modes in the orthorhombic $Pbnm$ perovskites. On the other hand, the quadratic-quadratic type interaction ($h_1 \neq 0$) rather than the linear-quadratic term is allowed for the coupling between B_g and B_u modes. The linear-quadratic (third-order) term leads to pure displacive coupling dynamics, while the quadratic-quadratic (fourth-order) term leads to four different dynamical regions.[28] For the third-order A_g-B_u coupling, the derivative of E with respect to the Raman amplitude is expressed as $\partial E/\partial Q_R = \nu_R^2 Q_R + a_3 Q_R^2 + a_4 Q_R^3 + gQ_{IR}^2$. Neglecting the non-coupled cubic and quartic Raman terms ($a_3, a_4 \sim 0$), which is a good approximation for a direct IR excitation, we find the energy minimum for the excited state occurs at a nonequilibrium value

$$Q_R^* = -\frac{gQ_{IR}^2}{\nu_R^2}. \quad (2)$$

We find from Eq. 2 that a larger displacive amplitude Q_R^* can be obtained by (i) increasing the interaction strength g that couples the active IR mode to the scattered Raman mode, (ii) increasing the amplitude Q_{IR} of the stimulated IR mode, and (iii) by decreasing the frequency of the anharmonically coupled Raman mode, ν_R^2. Similarly, for the quadratic-quadratic coupling one can find two energy minimums with restrictions on a_4 and h_1. The fourth order coupling strength is in general much smaller than that of the third order, which will be shown below. Thus in the current work we mainly focus on the $Q_{IR}^2 Q_R$ term.

With these different parameters available for nonlinear phononic control, we seek to understand how to enhance the coupling strength g to access the nonequilibrium state more efficiently. We anticipate that varying the chemistry of the A- or B-site cations in perovskite oxides will lead to differences in the IRS coupling strength through changes to the atomic masses, ionic radii, and the metal-oxygen bond stiffness (which is related to frequency of the normal modes). Which factor is the more important for controlling 'g' remains yet unknown.

Here we combine symmetry analyses with density functional theory (DFT) calculations to systematically investigate the microscopic dependencies of the IRS coupling strength in orthorhombic perovskites, focusing on variations in the A cation chemistry and band filling. We use $CaTiO_3$ (d^0) and $LaTiO_3$ (d^1) titanates as prototypical compounds. We find that the linear phononic properties are tuned by the A cation chemistry with the phonon mode frequencies in $CaTiO_3$ greater than those of $LaTiO_3$. We then obtain the linear-quadratic coupling strength g by fitting first-principles energy surfaces with respect to the mode amplitude and correlation strength to isolate the d orbital filling effect. First, the nonlinear coupling between IR and Raman modes is much larger than that between hyper-Raman and Raman modes, indicating IR modes to be more efficient driving modes. Furthermore, we find that the contribution of the driven IR mode to changes in the electronic structure cannot be neglected, although such perturbations to the bandwidth and band gap occur on different (shorter) timescale than the Raman-induced changes. The change of the valence bandwidth induced by the combined modes is equal to the sum of that from each individual mode, indicating that phonon-electron excitation remains in the perturbation region during this process. The difference in the nonlinear coupling g between CTO and LTO is more than 30%, which arises from a band filling effect and changes in the Ti–O bond stiffness; g is also weakly dependent on correlation strength.

The remainder of the article is organized as follows: Section II describes the compounds and methodology applied for calculating the nonlinear coupling strength. The main results appear in Section III, which is subdivided in to three parts: the linear lattice dynamical properties, the nonlinear coupled phonon properties, and the changes in electronic structures that occur due to the phononic processes. In Section IV, we discuss the factors that control the strength of the nonlinear interaction g and summarize our main results in Section V.
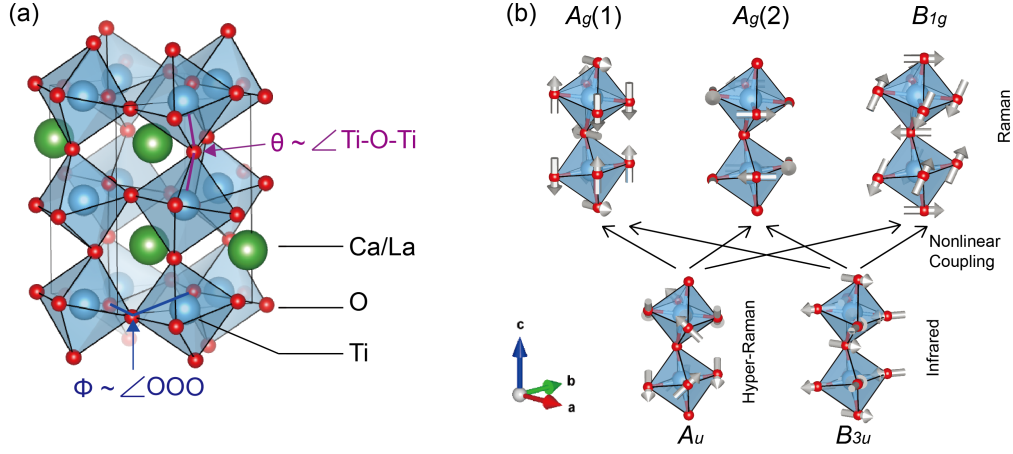
FIG. 1. (Color online) (a) Structure model of orthorhombic $CaTiO_3$ and $LaTiO_3$. The green spheres denote the A-site cations, Ca or La. The blue and red spheres denote the Ti and oxygen atoms, respectively. The octahedra tilting (ϕ) and rotational (θ) angles are defined as $\phi = (180° - \angle(Ti - O - Ti))/2$, and $\theta = (90° - \angle(OOO))/2$, where the Mn-O-Mn and interoctahedral O–O–O (denoted OOO) angles are showed following the convention introduced in Ref. [27]. (b) Illustration of the (upper panel) three Raman mode displacements (directions indicated by gray arrows) that are anharmonically coupled through a nonlinear interaction (black arrow) to the different symmetry (lower panel) hyper-Raman and IR modes explored in this work.

II. MATERIALS AND METHODS

A. Perovskite Oxide Titanates

Perovskite $CaTiO_3$ (CTO) and $LaTiO_3$ (LTO) are isostructural, exhibiting the orthorhombic *Pbnm* space group[29,30] with the $GdFeO_3$-type distortion. The TiO_6 octahedra rotate about the c axis (cooperatively in-phase, c^+), and tilt (in an out-of-phase sense, a^-a^-) about the pseudocubic [110] direction [Fig. 1(a)]. The lattice constants and octahedral rotational angles for CTO and LTO are given in Table I. The density functional calculated lattice constants are within 2% (see below for DFT details). The larger lattice parameters and rotational angles in LTO compared to CTO originate from the larger ionic radius of La compared to Ca.

The structural similarity of these two oxides allows us to isolate the intrinsic chemical effect on the nonlinear interaction. To exclude the volume and mass contribution to the phonon frequencies and more clearly identify the contribution from the change in orbital occupancy to g, we also electronically dope the systems to obtain hypothetical d^0 $LaTiO_3$, which we refer to as $(LTO)^{1+}$, and d^1 $CaTiO_3$, $(CTO)^{1-}$. We find that the one-electron difference has a significant effect on the cell volume and in turn the tilting angle in CTO and the rotation angle in LTO (Table I). Remarkably, the rotation angle in $(LTO)^{1+}$ is nearly suppressed manifests in the linear and nonlinear dynamical properties discussed in detail below.

B. Density Functional Calculations

DFT calculations were performed with the Vienna *Ab-Initio* Simulation Package (VASP)[31,32] with the projector augmented wave (PAW) method[33] to treat the core and valence electrons using the following electronic configurations: $3p^64s^2$ for Ca, $6s^25s^25p^65d^1$ for La, $3s^23p^63d^2$ for Ti, and $2s^22p^4$ for O. The revised Perdew-Burke-Ernzerhof exchange-correlation functional for solids (PBE-sol)[34] was selected as it gives accurate oxide lattice parameters. The Brillouin zone is sampled using an $8 \times 8 \times 6$ Γ-centered Monkhorst-Pack k-point mesh and integrations are performed using Gaussian smearing with a width of 10 meV. All structures were restricted to the observed *Pbnm* symmetry during structural optimization, whereby the lattice constants and atomic positions are relaxed until the stresses and forces on each atom are less than 3.5 kB and 0.1 meV Å^{-1}, respectively. Owing to correlated Ti-3d electrons, we used the plus Hubbard U method of Dudarev *et al*[35] with $U_{eff} = 4.4$ eV for LTO. Hereafter,

TABLE I. Structure parameters for bulk $CaTiO_3$ and $LaTiO_3$ and electronically doped $[CaTiO_3]^{1-}$ and d^1 $[LaTiO_3]^{1+}$ obtained from experiment (Exp.) and calculated in this work. Octahedral rotation (θ) and tilting (ϕ) are defined as in Fig. 1.

	a (Å)	b (Å)	c (Å)	θ (deg.)	ϕ (deg.)
$CaTiO_3$ (Exp.[29])	5.388	5.447	7.654	8.6	11.5
$CaTiO_3$ (this work)	5.370	5.497	7.661	9.7	14.0
$(CaTiO_3)^{1-}$	5.606	5.948	8.405	9.75	19.0
$LaTiO_3$ (Exp.[30])	5.630	5.584	7.901	9.20	12.7
$LaTiO_3$ (this work)	5.655	5.673	7.921	10.6	15.4
$(LaTiO_3)^{1+}$	5.367	5.270	7.433	0.10	10.6

TABLE II. Similarity S of Raman modes between $CaTiO_3$ and $LaTiO_3$. The numbers and labels in the first column (row) denote the phonon index and symmetry (sym.), respectively, in CTO (LTO).

CTO index (sym.)	LTO index (sym.)		
	5 (B_{1g})	9 (A_g)	12 (A_g)
5 (A_g)	0	0.26	0.77
6 (A_g)	0	0.92	0.33
9 (B_{1g})	0.98	0	0

U_{eff} is referred to as U. For consistency purposes, we also applied the same value of U to CTO despite it being a band insulator.

C. Lattice Dynamics

The phonon properties are calculated using the frozen phonon method implemented in PHONOPY.[36] For the orthorhombic structure with 20 atoms in the unit cell, there are 60 zone-center normal modes ($7A_g+8A_u+7B_{1g}+8B_{1u}+5B_{2g}+10B_{2u}+5B_{3g}+10B_{3u}$).[37] After calculating the phonon spectrum for CTO and LTO, we selected three Raman active phonon modes, two with A_g symmetry and one with B_{1g} symmetry, to couple with one IR-active B_{3u} and one hyper-Raman-active A_u mode, respectively [Fig. 1(b)], for reasons described below: The selected A_g and B_{1g} modes describe octahedral rotations with the main rotation axes for the the $A_g(1)$ and $A_g(2)$ modes occurring about the b and c crystal axes, respectively. The octahedral rotation axis for the B_{1g} mode is about an axis parallel to the orthorhombic [011] direction.

The A_u mode consists of two different types of distortions. First, oxygen displacements rumple the basal TiO_4-plane of the octahedron. The in-plane O-Ti-O bonds bend and are no longer 180°. The second distortion is a scissor-type motion between nearest oxygen atoms within an octahedron. In contrast, the B_{3u} mode is polar and results in an electric dipole along the a crystal axis owing to two equatorial oxygen atoms shifting towards the Ti cation while the other two equatorial oxygen atoms move away.

With the quasi-static approximation, the energy surface expanded in terms of coupled normal modes, $E(Q_1, Q_2)$ is obtained by distorting the equilibrium $Pbnm$ crystal structures along the eigen-displacement vectors of a coupled Raman and IR mode set with varying amplitude as determined from our DFT phonon calculations. In this notation, Q_1 is the Raman mode amplitude while Q_2 corresponds to the driving IR or hyper-Raman mode amplitude. The displacement amplitudes are renormalized in units of Å·amu$^{1/2}$ to be consistent with the definition introduced previously.[28]
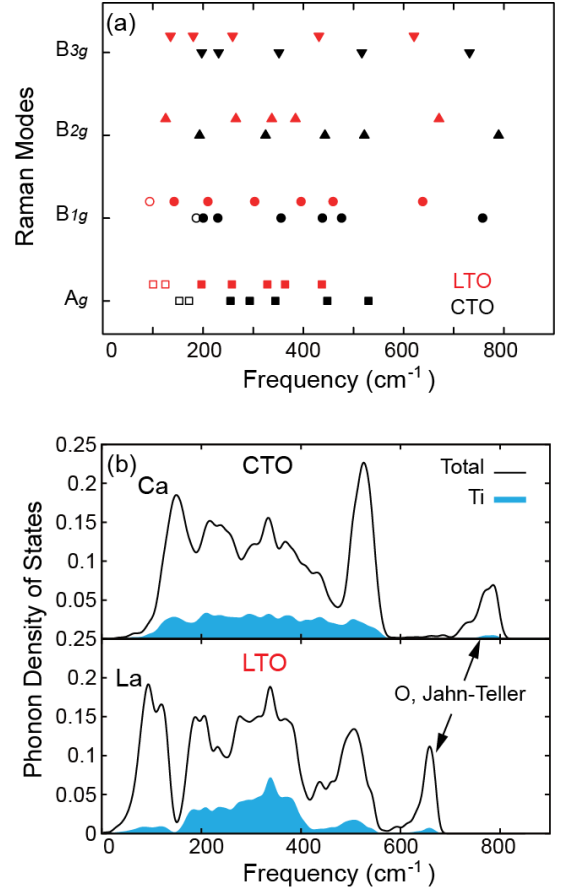

FIG. 2. (Color online) Lattice dynamical properties of $CaTiO_3$ and $LaTiO_3$ computed at the PBEsol+U level. (a) Frequency for the Raman active modes. The black and red points are for CTO and LTO, respectively. The selected A_g and B_{1g} Raman modes used to evaluate the the nonlinear coupling strength correspond to the empty symbols. (b) Phonon density of states (pDOS) for CTO and LTO. The black curve is the total pDOS whereas the filled blue curve shows the contribution from the Ti atoms. The Ti contribution to the lattice dynamical properties of CTO and LTO largely spans the frequency range from 150∼550 cm^{-1}, with small mixing from Ca/La at low frequency.

III. RESULTS

A. Linear Lattice Dynamical Properties

We first computed the zone-center phonon frequencies for both $CaTiO_3$ and $LaTiO_3$. Although the frequency and the ordering of modes in CTO and LTO are in general different, we identify similar modes by examining the irreducible representations (irrep) and the vibrational patterns using a similarity S overlap defined as $S = \mathbf{e}_i(CTO) \cdot \mathbf{e}_j(LTO)$, where $\mathbf{e}_{i,j}$ are the eigenvectors of the i-th normal mode,[38] listed in Table II. One can see that the mod character of LTO and CTO are not identical. The changes in structure and chemistry affect the interactomic forces and thus the eigenvectors. This behavior may be

TABLE III. Frequency (in cm^{-1}) for the selected lattice modes in perovskite titanates.

Mode	Activity	ν (CTO)	ν (LTO)	ν (CTO^{1-})	ν (LTO^{1+})
$A_g(1)$	R	152	125	115	188
$A_g(2)$	R	172	100	138	65
B_{1g}	R	187	94	125	40
A_u	hyper-R	440	364	310	510
B_{3u}	IR	552	545	478	757

quantified using the mode similarity, whereby a mixing mixing of the modes wihtin the same irrep is permitted. For example, mode index 5 (6) of CTO corresponds to the mode 12 (9) of LTO, which we denote herein as the $A_g(1)$ [$A_g(2)$] modes.

Fig. 2(a) shows the Raman frequencies for both titanates differentiated by mode symmetry; generally the mode frequencies for CTO (red symbols) are greater than those for LTO. This uniform shift in frequencies can be understood using a harmonic oscillator model with a frequency proportional to $\sqrt{J/M}$, where J is the spring constant and M is the normalized mass. Owing to the smaller atomic mass of Ca and the shorter and more covalent Ti-O bonds (J is larger in CTO than LTO) the CTO phonon frequencies are harder.

In Fig. 2(b) we plot the total and atom-resolved phonon density of states (pDOS) to identify the contributions from the Ti cations. The contributions from the A-site ions and oxide anions are also denoted explicitly in the figure. The effect from the A site mass difference on the pDOS at low frequency is clearly discernible. The Ti pDOS mainly spans the frequency range from 150 to 575 cm^{-1}. The Ti peak positions show good one-to-one correspondence between CTO and LTO, indicating that the linear dynamical properties derived from Ti in both phases should be rather similar despite the different formal oxidation state of Ti^{4+} and Ti^{3+}, respectively.

Finally at the high frequency end, we find a greater discrepancy in the pDOS of CTO and LTO, which originates from the TiO$_6$ octahedral breathing mode and the Jahn-Teller modes. For CTO these peaks span the frequency range from 700 to 810 cm^{-1}, while for LTO the corresponding modes occur in the range from 580 to 700 cm^{-1}. This difference occurs because the breathing and Jahn-Teller modes are very sensitive to the Ti-O bond lengths, *i.e.*, the TiO$_6$ octahedral volume, which is largely determined by the A cation radius in the perovskite titanates.

B. Nonlinear Anharmonic Coupling

Based on the IRS theory, when an IR mode is pumped intensely the Raman modes are coupled nonlinearly, vibrating about a nonequilibrium position. The displacive nonequilibrium position for a particular Raman mode depends on the coupling constant between the IR and the Raman modes.[15] In principle all symmetry-allowed

Raman modes should be excited through this process, however, a larger frequency difference between the IR and the Raman mode leads to more efficient coupling,[10] because the high frequency vibration of the IR mode can then be viewed as a constant force that shifts the Raman mode away from the original equilibrium value. A low frequency Raman mode is then preferred owing to the form of Eq. 1. Thus we focus on high frequency IR modes and low frequency Raman modes (Table III): The three Raman modes of lowest frequency include two A_g modes and one B_{1g} mode, which are coupled to a B_{3u} IR mode. An A_u mode is also included in our consideration as a driving mode for comparison. Although the A_u mode is not IR active, it can be excited through hyper-Raman scattering processes.

Fig. 3 shows the calculated energy surfaces for CTO and LTO with varying amplitude of the B_{3u} and the A_u modes. First, we find that the excitation of the B_{3u} mode drives the Raman mode into a nonequilibrium position for both titanates that depends on the excited IR mode amplitude according to Eq. 1. For example, with an excited B_{3u} mode ampltidue of 1.6 Å amu$^{1/2}$, the equilibrium $A_g(1)$ position shifts by ~ 0.8 Å amu$^{1/2}$ in CaTiO$_3$, corresponding to a maximum net atomic displacement of ~ 0.03 Å obtained by summing the displacements made by the four apical O atoms.

Next using our DFT energy surfaces, we parameterize Eq. 1 to obtain the coupling coefficients listed in Table IV. One can see that the coupling coefficients h_1 are very small compared to the lower-order leading terms in the energy expansion. The linear-quadratic couplings (g) dominate the nonlinear phononic coupling in these titanate systems and therefore we neglect the quadratic-quadratic interactions in the following discussion. With the coupling coefficients, we can predict the nonequilibrium energy minimum with Eq. 2, plotted as the inset in the left panel of Fig. 3. For LTO the energy minimum of both A_g modes is well predicted, while for CTO the energy minimum is underestimated by Eq. 2 for the $A_g(1)$ mode. This indicates higher order terms might be necessary for CTO.

The ability of the hyper-Raman A_u mode to drive the IRS coupling is much smaller. The largest coupling is to the $A_g(1)$ mode, with $g = 0.003$ for CTO and $g = 0.007$ for LTO, an order of magnitude smaller than that obtained by the B_{3u} mode. Under an A_u mode driving amplitude of 1.6 Å amu$^{1/2}$, the $A_g(1)$ mode is only driven 0.2 Å amu$^{1/2}$ from its equilibrium position, i.e. only one-forth of that achieved by the IR-active B_{3u} excitation. We find similar results for LaTiO$_3$. Our calculations show that the A_u mode is very inefficient for the purpose of nonlinear driving of Raman mode through IRS coupling.

C. Phonon-Induced Electronic Structure Changes

The objective of using nonlinear phononic coupling to induce a transient structure exhibiting nonequilibrium electronic and magnetic properties relies on a low fre-
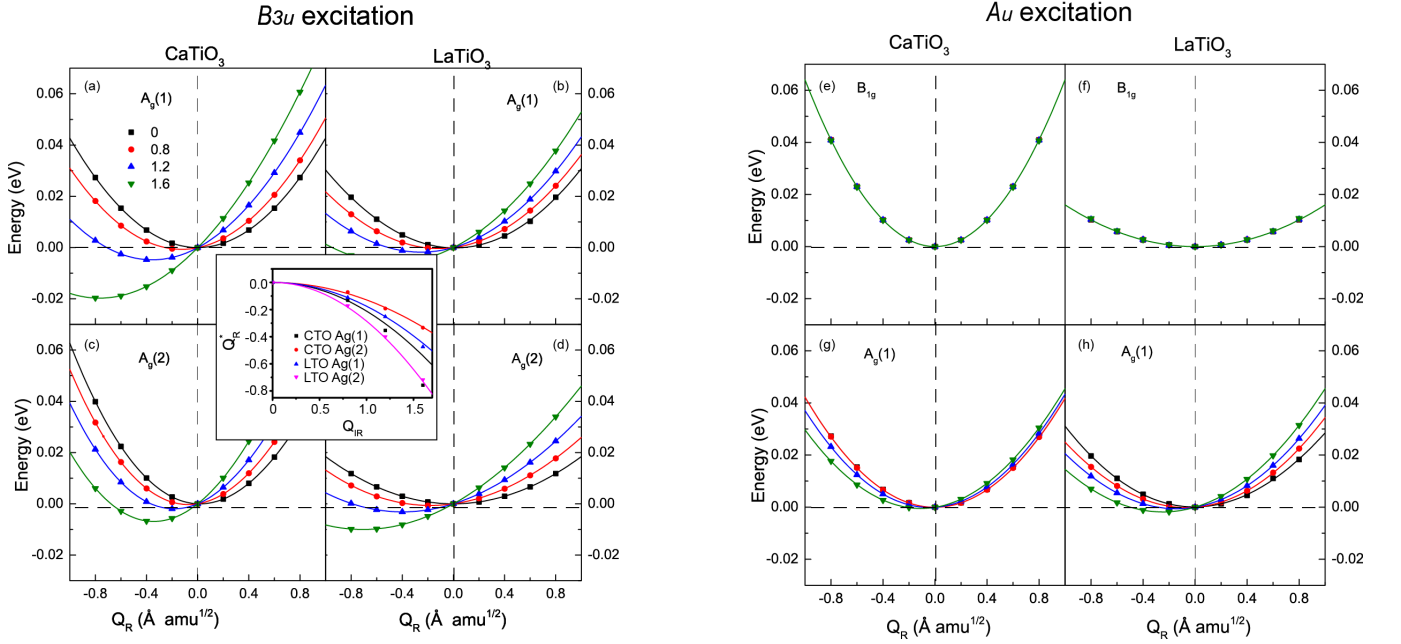
FIG. 3. (Color online) Energy profiles for the nonlinear coupling between two phonon modes. Left panels: (a-d) Energy profiles for the two A_g modes under the excitation of the IR B_{3u} mode in CTO and LTO. Right panels: (e-h) Energy profiles for the B_{1g} mode and the two A_g modes under the excitation of the hyper-Raman A_u mode. Note that in the upper panels all curves are overlapping, indicating that the B_{1g} mode is decoupled from the A_u mode by symmetry. Note that here we show $A_g(1)$ mode for CTO and $A_g(2)$ mode for LTO, because the corresponding couplings are stronger. The inset in the left panel shows the predicted Q_R^* dependence on the IR mode amplitude from Eq. 2 (curves) and the DFT computed data (symbols).

TABLE IV. Coupling coefficients for pairs of interacting phonons in CaTiO$_3$ (CTO) and LaTiO$_3$ (LTO) obtained from the DFT computed energy surfaces fit to the polynomial phononic coupling expression given in Eq. 1.

	Coupled modes (Q_1, Q_2)	a_3	b_4	g	h_1
CTO	$(A_g(1), B_{3u})$	-0.002	0.029	0.018	-
	$(A_g(2), B_{3u})$	-0.013	0.029	0.014	-
	$(A_g(1), A_u)$	-0.001	0.003	0.003	-
	(B_{1g}, B_{3u})	-0.004	-5×10^{-5}	-	-3.4×10^{-4}
	(B_{1g}, A_u)	-4.7×10^{-4}	5.2×10^{-4}	-	-4.1×10^{-4}
LTO	$(A_g(1), B_{3u})$	-0.001	0.032	0.010	-
	$(A_g(2), B_{3u})$	-0.002	0.032	0.011	-
	$(A_g(1), A_u)$	-0.003	0	0.007	-
	(B_{1g}, B_{3u})	-0.001	0	-	-6.1×10^{-5}
	(B_{1g}, A_u)	-0.002	9.2×10^{-5}	-	-8.1×10^{-4}

quency Raman mode vibrating about a position displaced from equilibrium. For example, in YBa$_2$Cu$_3$O$_{6.5}$ the distorted Raman mode leads to the reduction in the Cu-O bond distance which could favor the superconducting state,[15] while in PrMnO$_3$ the nonequilibrium amplitude of the Raman mode reduces the octrahedra rotation angles towards a psudocubic phase and therefore is supposed to tend to drive the system to a metallic phase.[28] The hypothesis in all of these scenarios is that after the nonlinear excitation any observed changes in the material properties are mainly due to the nonequilibrium Raman mode amplitude with the driven IR mode playing a minor in dictating the properties (albeit it provides a route to

active them). We now examine this idea for the driven IR-active B_{3u} mode coupled to the $A_g(1)$ Raman mode.

First, we note that CTO and LTO exhibit distinct electronic structures from each other owing to the difference in band filling. In our PBEsol+U calculations, the d^0 band insulator CTO has a large band gap, ~ 2.8 eV while d^1 LTO is a Mott insulator with a small gap of ~ 1.7 eV.[39,40] The electronic density of states (DOS) are plotted in Fig. 4. The size of band gap in LTO highly depends on the correlation strength, U, and the experimental optical gap is 0.1$\sim$0.2 eV. In terms of the band gap, our DFT calculations more accurately describe CTO than LTO; however, because the main effect of the DFT+U formalism for the titanates is to provide a rigid shift of the conduction band, the trends we observe in phonon-driven band gap changes is reliable and can be used as a reference for the future experiments.

We find that neither the excited $A_g(1)$ nor B_{3u} mode produce any significant changes in the electronic band gap in CTO [Fig. 4(b,c)]. Instead, we find that the main effect is to increase the valence bandwidth with the $A_g(1)$ mode less effective (increase of ~ 30 meV) than the B_{3u} mode (increase of ~ 170 meV). Next, when the two modes are coupled together through the nonlinear interaction with amplitudes corresponding to the optimal nonequilibrium structure [Fig. 4(d)], the increase in the valence bandwidth is greater (~ 200 meV), and the bandgap is reduced by ~ 60 meV. The change of the valance bandwidth W for the combined modes is equal to the sum of the individual
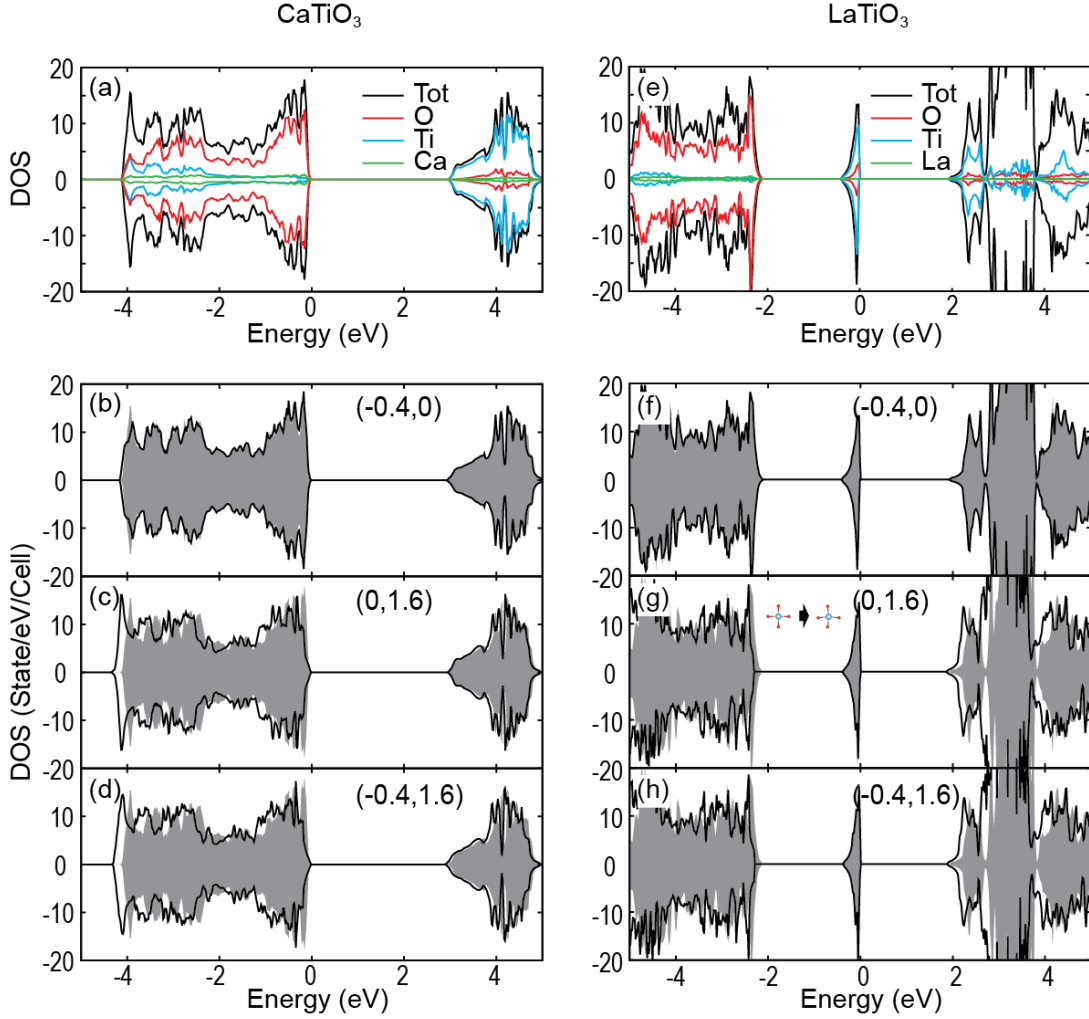
FIG. 4. (Color online) Electronic densities of states (DOS) for the (a) and (e) equilibrium CaTiO$_3$ and LaTiO$_3$ structure, (b,c) and (f,g) singly excited B_{3u} mode, and (d,h) couped excited modes with corresponding amplitudes given in parentheses for each mode as $(Q(A_g(1)), Q(B_{3u}))$ in units of Å amu$^{1/2}$ for CTO (panels b-d) and LTO (panels (f-h). In panels (a) and (e), the total and the atom-projected DOS are provided. The equilibrium DOS is also shown in the gray shaded region.

modes, i.e. $\Delta W(\Delta Q_1, \Delta Q_2) = \Delta W(\Delta Q_1) + \Delta W(\Delta Q_2)$, which indicates that both phonon excitations can be regarded as independent perturbations to the electronic energy levels. This 'sum rule' can be used to identify the contribution to the experimental spectrum shift from the coupled modes.

In LTO, the nonequilibrium Raman mode itself does not show any obvious effect on the electronic structure, while the IR mode lowers the energy of all the states except the lower Hubbard band by ~ 0.13 eV, including at the valence band (-6.1 eV ~ -2.2 eV) and conduction band (> 1.8 eV). The lower Hubbard band, ranging from -0.3 eV ~ 0 eV and consisting of the non-bonding Ti-t_{2g} states, largely remains unchanged under the modulation of both modes. Since the x-axis in Fig. 4 is the relative energy with respect to the Fermi level, which is determined by the lower Hubbard band, the down-shift of all the bands except the lower Hubbard band should be understood as

a shift of the lower Hubbard band to higher energy.

To understand why the IR mode increases the energy of the lower Hubbard band we examine the local distortion to the TiO$_6$ octahedra by this mode, illustrated in the inset of Fig. 4. The lower Hubbard band is constructed from one electron occupying the t_{2g} orbital, which forms a nonbonding interaction with the oxide anions. The angular component of this orbital makes it sensitive to the Coulomb repulsion induced by the octahedral distortion. The IR mode induced acentric distortion affects all three t_{2g} orbitals in a similar manner by bending the O-Ti-O bonds. The increased electrostatic energy cannot be reduced by redistributing the electron through a change in orbital polarization,[14] resulting in a shift of the t_{2g} energy to higher energy.

Based on the above comparison, we find that the contribution from the IR mode in changing the electronic structure is significant. During the IRS process, the IR

mode vibrates at a much higher frequency compared to the Raman mode. Therefore its induced electronic structure modulation occurs on a shorter time scale compared to that obtained from the Raman mode. Also, the IR-active mode induced changes should appear as a periodic vibrational modulation rather than a stationary one induced by the displacive Raman mode. However since its effect to the DOS is much prominent, one should be careful when assigning mode contributions to macroscopic electronic-related properties.

D. Role of Orbital Filling

In order to examine the effect of band filling, we computed the dynamical responses for electron doped and hole doped $CaTiO_3$ and $LaTiO_3$, by artificially adding electrons/holes to each material, effectively shifting the chemical potential, in the DFT calculation. In this way the $3d$ band occupancies n range from $n = 0$ to 1, which allows us to isolate the orbital filling effect from those due to explicit changes to the structure from the Ca or La chemistry. The results are shown in Fig. 5. Upon increasing the orbital occupancy from d^0 to d^1, the volume, orthorhombicity b/a, and both rotation and tilt angles increase. The most significant effect is on the $LaTiO_3$ tilt angle, which is completely suppressed when the hole concentration exceeds 50% (Fig. 5(c)).

Furthermore, the change in linear phonon properties is reflected in the frequencies of the normal modes, which shift to lower wavenumber upon filling the orbital, see Fig. 5(e) and Fig. 5(f). The A_g and B_{1g} frequencies of $[CTO]^{1-}$ are close to that of LTO. This effect is a consequence of electrons filling the antibonding t_{2g} manifold, which reduces the Ti-O bond stiffness and hence the relevant force constants. This is also consistent with the increase in the Ti-O bond length as electrons occupy this manifold.

Finally, the nonlinear coupling coefficient g between the $A_g(1)$ and the B_{3u} modes with orbital filling is shown in Fig. 5(g). Compared to the pristine compound, $[LTO]^{1+}$ shows a 29% increase in g while for $[CTO]^{1-}$ g decreases by 35%, both of which become closer to the counterpart undoped system, respectively. Therefore, we deduce that the variation in nonlinear coupling strength between these two systems are mainly governed by the orbital filling. Fig. 5 shows that generally both the phonon mode frequencies and the nonlinear coupling coefficients decrease as the number of electrons in the t_{2g} orbital increases. Furthermore, the higher the frequencies of the coupled phonon modes, then the larger the coupling coefficient that can be achieved. Such interdependence between the nonlinear coupling coefficient g and the linear phonon properties will be explained in the following discussion. Last, a linear interpolation between the two end members provides an adequate estimate of the effect of electronic doping the d^n system.
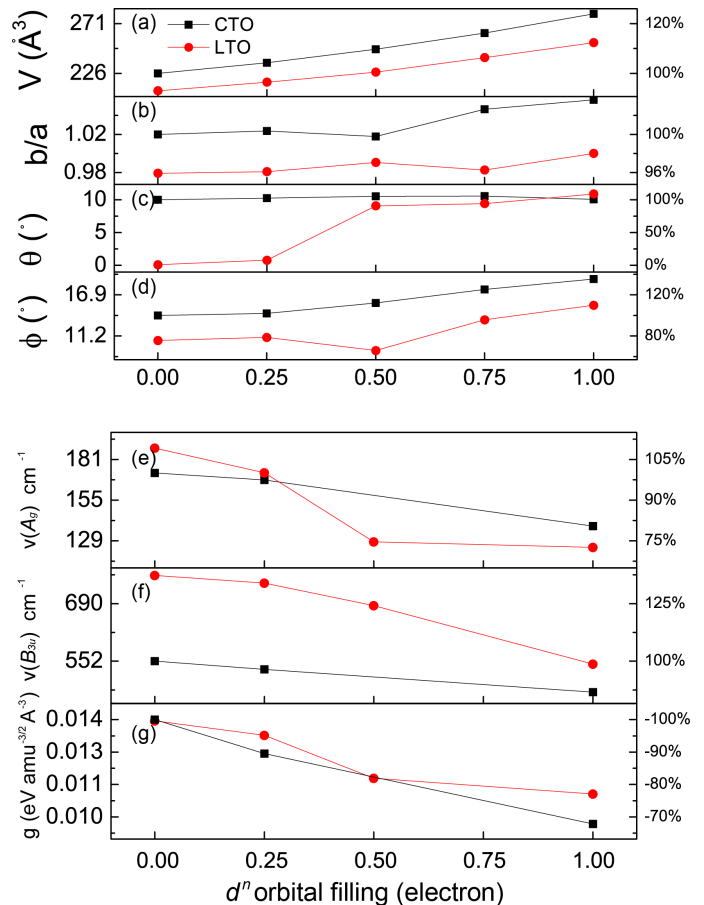

FIG. 5. (Color online) (a-d) Structural parameters and (e-g) lattice dynamical properties with respect to the number of electrons in the Ti $3d$ manifold. d^0 corresponds to undoped $CaTiO_3$ (black, squares) and holed doped $[LTO]^{1+}$ (red, circles) whereas d^1 corresponds to undoped $LaTiO_3$ and electron doped $[CTO]^{1-}$. A quantitative measure of changes in these parameters with the orbital filling is given as a percentage relative to the original bulk values of CTO. Panel (g) clearly shows that the additional one electron quantitatively reduces the nonlinear coupling strength g by $\sim 32\%$.

IV. DISCUSSION

A. Nonlinearity Between Modes

To further understand the presented results, we now explore the atomistic origin of the coupling coefficient g describing the nonlinear interaction between phonons. First, recall that the change in potential energy induced by a phonon mode can originate from two parts: changes in bond lengths and/or bond angles. The second contribution, which is proportional to the cosine of the bond angle, is often minor compared to variations in the bond length. Here we focus on the bond length contribution.

The potential energy as a function of interatomic distance is not parabolic in the anharmonic regime. The parabolic approximation is only valid near equilibrium.
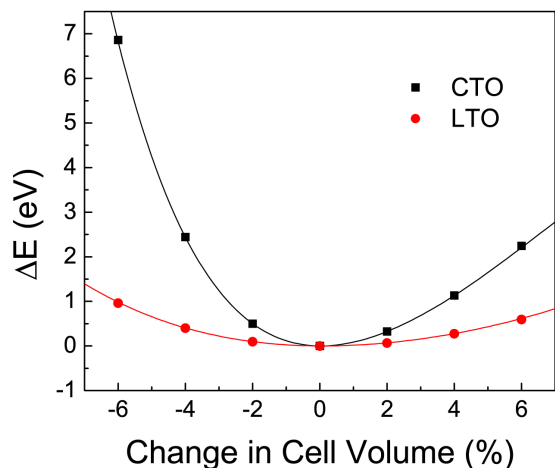
FIG. 6. (Color online) CaTiO$_3$ and LaTiO$_3$ equations of state. The third through fifth order terms of CTO are more than one order-of-magnitude larger than those of LTO.

The more the bond length deviates away from the equilibrium position, the greater the anharmonic contributions to the energy surface. For a family of compounds with the same local chemistry (Ti and O) in the titanate oxides explored, if a given mode amplitude can drive one compound further away from the equilibrium than the other, then the anharmonic coupling should be larger in the former material. This behavior is indicative of a larger bond stiffness, which provides for the larger nonlinear coupling coefficient and explains why in Fig. 5 the coupling coefficient g is correlated to the phonon mode frequency. Indeed, the equation of state for both materials shows that the higher order terms are more significant in CTO compared to LTO (Fig. 6), together with a larger Ti–O bond stiffness. In an octahedral ligand field, the filling of the t_{2g} in general increases the Ti-O bond lengths through electrostatic Coulomb repulsion, and weakens the bond stiffness. Therefore as the orbital filling increases, both the phonon mode frequency and the nonlinear phononic coupling coefficient decrease. This conceptual picture clarifies the observation that g(CTO) $> g$(LTO). Such effect is similar to the mechanism of phononic anharmonicity in one-dimensional diatomic chains.[41–43]

B. Electron Correlation Effects

Here we examine the effect of correlation strength, included in our PBEsol+U DFT calculations through the Hubbard U corrections, on the linear and nonlinear lattice dynamical properties. Using LaTiO$_3$ as an example, Fig. 7(a) shows the phonon normal mode frequencies with respect to U. The U-dependence for all selected Raman modes is weak. This is because these modes mainly correspond to octahedra rotations, which are largely insensitive to the on-site electron localization at metal center.[44] On the other hand, electron correlation localizes the electron

in the t_{2g} orbitals, reducing the Ti–O bond length, and can harden those IR modes that directly alter the Ti–O bond length [Fig. 7(b)]. For example, the resulting change in the B_{3u} frequency with respect to U is 5.68 (cm·eV)$^{-1}$ for CTO and 5.22 (cm·eV)$^{-1}$ for LTO.

Interestingly, there is a high frequency Raman mode in LTO which has a frequency rapidly decreases with an increasing U [Fig. 7(a), red data]. By examining the atomic displacement pattern for this mode, we identified it as a Q_3 Jahn-Teller mode. This mode alternatively increases/decreases the amplitude of the Q_3 Jahn-Teller distortion (two-out–four-in bond stretching) of neighboring TiO$_6$ octahedra, further lifting the degeneracy of the t_{2g} orbitals and producing an orbital polarization.[14,45] The electron correlation localizes the t_{2g} electron on one orbital and therefore softens the Q_3 phonon.[14]

The energy surfaces under different value of U and the coupling constant were computed (not shown here). We find that the correlation strength U is not a principal factor in determining the strength of the nonlinear coupling [Fig. 7(c)]. The variation of the coupling constant Δg over $0 < U < 4.4$ eV is less then 6×10^{-4} eV Å^{-3} amu$^{-3/2}$, which is essentially negligible. In fact, in the explored titanates electron correlation only weakly alters the Ti-O-Ti bond angle and bond length.[46] Thus correlation effects act as a higher order perturbation to the energy surface. In summary, the electron correlation is negligible for the nonlinear phononic coupling and does not change the conclusions on our comparative study in perovskite titanates.

V. CONCLUSIONS

We performed DFT calculations on the d^0 CaTiO$_3$ (CTO) and d^1 LaTiO$_3$ (LTO) titanates to understand the microscopic origin of the nonlinear phononic coupling coefficients. First, we found that the third-order linear-quadratic coupling is more important than the quadratic-quadratic interactions in perovskite titanates. The linear-quadratic coupling of CTO is larger than that for LTO by as much as $\sim 30\%$, which we attribute mainly to the difference in electron filling. The electrostatic repulsion induced by increasing the filling within the t_{2g} manifold elongates the Ti-O bond lengths, resulting in reduced bond stiffness and lattice anharmonicity which act to reduce the coupling coefficients. This correlation between the bond stiffness and the nonlinear coupling coefficients appears to be general, at least for t_{2g} systems, but requires further investigation in e_g active compounds. This understanding can be used as guide to select materials with large anharmonicities to more readily explore nonequilibrium phases with experimentally accessible ionic Raman scattering approaches.
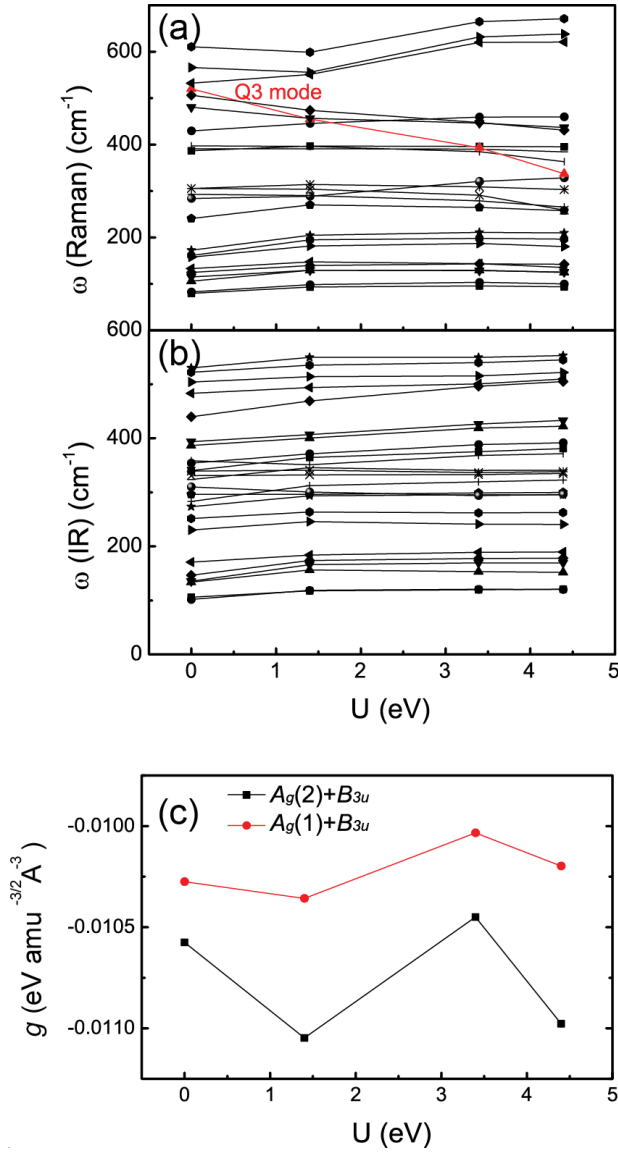
FIG. 7. (Color online) Effect of electron correlation to the linear (a-b) and nonlinear (c) phonon properties of LaTiO$_3$. There is no clear trend for the changes in nonlinear coupling strength with correlation strength; the variation over the U range explored is within 5%.

* jrondinelli@northwestern.edu

[1] M. Forst, C. Manzoni, S. Kaiser, Y. Tomioka, Y. Tokura, R. Merlin, and A. Cavalleri, "Nonlinear phononics as an ultrafast route to lattice control," Nat Phys **7**, 854–856 (2011), 10.1038/nphys2055.

[2] A. R. Khorsand, M. Savoini, A. Kirilyuk, A. V. Kimel, A. Tsukamoto, A. Itoh, and Th Rasing, "Role of magnetic circular dichroism in all-optical magnetic recording," Physical Review Letters **108**, 127205 (2012).

[3] C. D. Stanciu, F. Hansteen, A. V. Kimel, A. Kirilyuk, A. Tsukamoto, A. Itoh, and Th Rasing, "All-optical magnetic recording with circularly polarized light," Physical

Review Letters **99**, 047601 (2007).

[4] Matteo Rini, Ra'anan Tobey, Nicky Dean, Jiro Itatani, Yasuhide Tomioka, Yoshinori Tokura, Robert W. Schoenlein, and Andrea Cavalleri, "Control of the electronic phase of a manganite by mode-selective vibrational excitation," Nature **449**, 72–74 (2007).

[5] A. V. Kimel, A. Kirilyuk, A. Tsvetkov, R. V. Pisarev, and Th Rasing, "Laser-induced ultrafast spin reorientation in the antiferromagnet TmFeO$_3$," Nature **429**, 850–853 (2004), 10.1038/nature02659.

[6] J. A. de Jong, A. V. Kimel, R. V. Pisarev, A. Kirilyuk, and Th Rasing, "Laser-induced ultrafast spin dynamics in

ErFeO$_3$," Physical Review B **84**, 104421 (2011).

[7] R. V. Mikhaylovskiy, E. Hendry, A. Secchi, J. H. Mentink, M. Eckstein, A. Wu, R. V. Pisarev, V. V. Kruglyak, M. I. Katsnelson, Th Rasing, and A. V. Kimel, "Ultrafast optical modification of exchange interactions in iron oxides," Nat Commun **6** (2015).

[8] C. Manzoni, M. Forst, H. Ehrke, and A. Cavalleri, "Single-shot detection and direct control of carrier phase drift of mid-infrared pulses," Opt. Lett. **35**, 757–759 (2010).

[9] M. Forst, R. Mankowsky, and A. Cavalleri, "Mode-selective control of the crystal lattice," Accounts of Chemical Research **48**, 380–387 (2015).

[10] R. Mankowsky, M. Först, T. Loew, J. Porras, B. Keimer, and A. Cavalleri, "Coherent modulation of the YBa$_2$Cu$_3$o$_{6+x}$ atomic structure by displacive stimulated ionic raman scattering," Phys. Rev. B **91**, 094308 (2015).

[11] M. Forst, R. I. Tobey, S. Wall, H. Bromberger, V. Khanna, A. L. Cavalieri, Y. D. Chuang, W. S. Lee, R. Moore, W. F. Schlotter, J. J. Turner, O. Krupin, M. Trigo, H. Zheng, J. F. Mitchell, S. S. Dhesi, J. P. Hill, and A. Cavalleri, "Driving magnetic order in a manganite by ultrafast lattice excitation," Physical Review B **84**, 241104 (2011).

[12] R. Singla, G. Cotugno, S. Kaiser, M. Först, M. Mitrano, H. Y. Liu, A. Cartella, C. Manzoni, H. Okamoto, T. Hasegawa, S. R. Clark, D. Jaksch, and A. Cavalleri, "Thz-frequency modulation of the hubbard u in an organic mott insulator," Phys. Rev. Lett. **115**, 187401 (2015).

[13] D. M. Kennes, E. Y. Wilner, D. R. Reichman, and A. J. Millis, "Electronic Squeezing of Pumped Phonons: Negative U and Transient Superconductivity," ArXiv e-prints (2016), arXiv:1609.03802 [cond-mat.supr-con].

[14] Mingqiang Gu and James M. Rondinelli, "Ultrafast band engineering and transient spin currents in antiferromagnetic oxides," Scientific Reports **6**, 25121 (2016).

[15] R. Mankowsky, A. Subedi, M. Forst, S. O. Mariager, M. Chollet, H. T. Lemke, J. S. Robinson, J. M. Glownia, M. P. Minitti, A. Frano, M. Fechner, N. A. Spaldin, T. Loew, B. Keimer, A. Georges, and A. Cavalleri, "Nonlinear lattice dynamics as a basis for enhanced superconductivity in YBa$_2$Cu$_3$O$_{6.5}$," Nature **516**, 71–73 (2014).

[16] M. A. Sentef, A. F. Kemper, A. Georges, and C. Kollath, "Theory of light-enhanced phonon-mediated superconductivity," Physical Review B **93**, 144506 (2016).

[17] Aavishkar A. Patel and Andreas Eberlein, "Light-induced enhancement of superconductivity via melting of competing bond-density wave order in underdoped cuprates," Physical Review B **93**, 195139 (2016).

[18] W. Hu, S. Kaiser, D. Nicoletti, C. R. Hunt, I. Gierz, M. C. Hoffmann, M. Le Tacon, T. Loew, B. Keimer, and A. Cavalleri, "Optically enhanced coherent transport in YBa$_2$Cu$_3$O$_{6.5}$ by ultrafast redistribution of interlayer coupling," Nat Mater **13**, 705–711 (2014).

[19] S. Kaiser, C. R. Hunt, D. Nicoletti, W. Hu, I. Gierz, H. Y. Liu, M. Le Tacon, T. Loew, D. Haug, B. Keimer, and A. Cavalleri, "Optically induced coherent transport far above T_c in underdoped YBa$_2$Cu$_3$O$_{6+\delta}$," Physical Review B **89**, 184516 (2014).

[20] M. Mitrano, A. Cantaluppi, D. Nicoletti, S. Kaiser, A. Perucchi, S. Lupi, P. Di Pietro, D. Pontiroli, M. Ricco, S. R. Clark, D. Jaksch, and A. Cavalleri, "Possible light-induced superconductivity in K$_3$C$_{60}$ at high temperature," Nature **530**, 461–464 (2016).

[21] N. A. Spaldin D. M. Juraschek, M. Fechner, "Ultrafast structure switching through nonlinear phonoics," ArXiv e-prints (2016), arXiv:1607.01653v1 [cond-mat.supr-con].

[22] Alaska Subedi, "Proposal for ultrafast switching of ferroelectrics using midinfrared pulses," Physical Review B **92**, 214303 (2015).

[23] E. K. H. Salje and M. A. Carpenter, "Linearquadratic order parameter coupling and multiferroic phase transitions," Journal of Physics: Condensed Matter **23**, 462202 (2011).

[24] Roman Mankowsky, Michael Frst, and Andrea Cavalleri, "Non-equilibrium control of complex solids by nonlinear phononics," Reports on Progress in Physics **79**, 064503 (2016).

[25] R. F. Wallis and A. A. Maradudin, "Ionic raman effect. ii. the first-order ionic raman effect," Phys. Rev. B **3**, 2063–2075 (1971).

[26] T. P. Martin and L. Genzel, "Ionic raman scattering and ionic frequency mixing," physica status solidi (b) **61**, 493–502 (1974).

[27] A. T. Zayak, X. Huang, J. B. Neaton, and Karin M. Rabe, "Structural, electronic, and magnetic properties of SrRuO$_3$ under epitaxial strain," Physical Review B **74**, 094104 (2006).

[28] Alaska Subedi, Andrea Cavalleri, and Antoine Georges, "Theory of nonlinear phononics for coherent light control of solids," Physical Review B **89**, 220301 (2014).

[29] R. H. Buttner and E. N. Maslen, "Electron difference density and structural parameters in CaTiO$_3$," Acta Crystallographica Section B **48**, 644–649 (1992).

[30] Manfred Eitel and J. E. Greedan, "A high resolution neutron diffraction study of the perovskite LaTiO$_3$," Journal of the Less Common Metals **116**, 95–104 (1986).

[31] G. Kresse and J. Furthm´uller, "Efficiency of ab-initio total energy calculations for metals and semiconductors using a plane-wave basis set," Computational Materials Science **6**, 15–50 (1996).

[32] G. Kresse and D. Joubert, "From ultrasoft pseudopotentials to the projector augmented-wave method," Phys. Rev. B **59**, 1758–1775 (1999).

[33] P. E. Blöchl, "Projector augmented-wave method," Phys. Rev. B **50**, 17953–17979 (1994).

[34] M. Ropo, K. Kokko, and L. Vitos, "Assessing the perdew-burke-ernzerhof exchange-correlation density functional revised for metallic bulk and surface systems," Phys. Rev. B **77**, 195445 (2008).

[35] S. L. Dudarev, L.-M. Peng, S. Y. Savrasov, and J.-M. Zuo, "Correlation effects in the ground-state charge density of Mott insulating NiO: A comparison of ab initio calculations and high-energy electron diffraction measurements," Phys. Rev. B **61**, 2506–2512 (2000).

[36] A Togo and I Tanaka, "First principles phonon calculations in materials science," Scr. Mater. **108**, 1–5 (2015).

[37] Mohammad A Islam, James M Rondinelli, and Jonathan E Spanier, "Normal mode determination of perovskite crystal structures with octahedral rotations: theory and applications," Journal of Physics: Condensed Matter **25**, 175902 (2013).

[38] P. Hermet, M. Veithen, and Ghosez Ph, "First-principles calculations of the nonlinear optical susceptibilities and raman scattering spectra of lithium niobate," Journal of Physics: Condensed Matter **19**, 456202 (2007).

[39] E. Pavarini, S. Biermann, A. Poteryaev, A. I. Lichtenstein, A. Georges, and O. K. Andersen, "Mott transition and

suppression of orbital fluctuations in orthorhombic $3d^1$ perovskites," Physical Review Letters **92**, 176403 (2004).

[40] E. Pavarini, A. Yamasaki, J. Nuss, and O. K. Andersen, "How chemistry controls electron localization in $3d^1$ perovskites: a wannier-function study," New Journal of Physics **7**, 188 (2005).

[41] A. M. Kosevich and A. S. Kovalev, "Self-localization of vibrations in a one-dimensional anharmonic chain," Sov. Phys. JETP **40**, 891 (1974).

[42] S. A. Kiselev, S. R. Bickham, and A. J. Sievers, "Anharmonic gap modes in a perfect one-dimensional diatomic lattice for standard two-body nearest-neighbor potentials," Phys. Rev. B **48**, 13508–13511 (1993).

[43] Yu. A. Kosevich, L. I. Manevitch, and A. V. Savin, "Wandering breathers and self-trapping in weakly coupled nonlinear chains: Classical counterpart of macroscopic tunneling quantum dynamics," Phys. Rev. E **77**, 046603 (2008).

[44] Antonio Cammarata and James M. Rondinelli, "Covalent dependence of octahedral rotations in orthorhombic perovskite oxides," The Journal of Chemical Physics **141**, 114704 (2014), http://dx.doi.org/10.1063/1.4895967.

[45] E. Pavarini, A. Yamasaki, J. Nuss, and O. K. Andersen, "How chemistry controls electron localization in $3d^1$ perovskites: a wannier-function study," New Journal of Physics **7**, 188 (2005).

[46] I. V. Solovyev, "Lattice distortion and magnetic ground state of $YTiO_3$ and $LaTiO_3$," Physical Review B **69**, 134403 (2004).